

# APPLICATION OF ATTOSECOND TECHNIQUES TO CONDENSED MATTER SYSTEMS

DISSERTATION

Presented in Partial Fulfillment of the Requirements for the Degree Doctor of  
Philosophy in the Graduate School of The Ohio State University

By

Gregory J. Smith, M.Sc.

Graduate Program in Physics

The Ohio State University

2019

Dissertation Committee:

Louis F. DiMauro, Advisor

L. Robert Baker

Jay A. Gupta

Yuri V. Kovchegov

© Copyright by

Gregory J. Smith

2019

# ABSTRACT

Lorem ipsum dolor sit amet, consectetuer adipiscing elit. Ut purus elit, vestibulum ut, placerat ac, adipiscing vitae, felis. Curabitur dictum gravida mauris. Nam arcu libero, nonummy eget, consectetuer id, vulputate a, magna. Donec vehicula augue eu neque. Pellentesque habitant morbi tristique senectus et netus et malesuada fames ac turpis egestas. Mauris ut leo. Cras viverra metus rhoncus sem. Nulla et lectus vestibulum urna fringilla ultrices. Phasellus eu tellus sit amet tortor gravida placerat. Integer sapien est, iaculis in, pretium quis, viverra ac, nunc. Praesent eget sem vel leo ultrices bibendum. Aenean faucibus. Morbi dolor nulla, malesuada eu, pulvinar at, mollis ac, nulla. Curabitur auctor semper nulla. Donec varius orci eget risus. Duis nibh mi, congue eu, accumsan eleifend, sagittis quis, diam. Duis eget orci sit amet orci dignissim rutrum.

Nam dui ligula, fringilla a, euismod sodales, sollicitudin vel, wisi. Morbi auctor lorem non justo. Nam lacus libero, pretium at, lobortis vitae, ultricies et, tellus. Donec aliquet, tortor sed accumsan bibendum, erat ligula aliquet magna, vitae ornare odio metus a mi. Morbi ac orci et nisl hendrerit mollis. Suspendisse ut massa. Cras nec ante. Pellentesque a nulla. Cum sociis natoque penatibus et magnis dis parturient montes, nascetur ridiculus mus. Aliquam tincidunt urna. Nulla ullamcorper vestibulum turpis. Pellentesque cursus luctus mauris.

Dedicated to ???

# ACKNOWLEDGMENTS

steve hageman - most work in this thesis was done in close collaboration with steve. major components of beamline were designed solely by steve, and he was there to help in nearly every single experiment. endless discussions on nearly every aspect of all experimental and design work.

andrew piper - OMRON safety system. attempt at interferometric stabilization

dietrich keissewetter - wrote the motor software, beamline pointing software out of the spitfire. helped with the initial design of the TABLE apparatus. helped chase down vibrations and make subtle improvements to the TABLE.

kent talbert - wrote the andor labview software, interfaced with the motors.

sierra o'bryan - optical design of the photon spectrometer

antoine camper - phase plate stuff.

tim gorman - endless discussions about physics, experimental design, laser troubleshooting

eric moore - laser pointing system.

pete at the machine shop - general machining help.

michael graham - mike helped with the design of the cage and crank, and had very useful tips and input for designing most mechanical systems.

jon the welder - he welded the spectrometer and mirror chambers, made modifications to the generation chamber, welded the high pressure cell input line.

Lou DiMauro - of course

# VITA

2010 .....	B.S., SUNY Stony Brook, Stony Brook, NY
2010 - 2012 .....	Research Analyst, Correlated Electron Group, Condensed Matter Physics and Materials Science Division at Brookhaven National Laboratory, Upton, NY
2014 .....	M.S., Ohio State University, Columbus, OH

## Publications

“Constraints on the Diffuse High-Energy Neutrino Flux from the Third Flight of ANITA”, P. W. Gorham, P. Allison, **O. Banerjee** *et al.*, Physical Review D. I am a lead author and contributor of the new binned analysis presented, which is one of the three complementary analyses in the paper. [Link to electronic version](#).

“Dynamic tunable notch filters for the Antarctic Impulsive Transient Antenna (ANITA)”, P. Allison, **O. Banerjee** *et al.*, Nuclear Instruments and Methods A. I led this paper and served as **corresponding author**. This paper is on the filters that I played a lead role in commissioning for ANITA-4, that helped to triple the livetime of the experiment. [Link to electronic version](#).

I am also a co-author on all ANITA publications (6 total) since Jan 2016.

## Fields of Study

Major Field: Physics

Studies in Particle Astrophysics: Connolly group

# Table of Contents

	Page
Abstract . . . . .	ii
Dedication . . . . .	iii
Acknowledgments . . . . .	iv
Vita . . . . .	v
<b>List of Figures</b> . . . . .	viii
<b>List of Abbreviations</b> . . . . .	x

## Chapters

<b>1 Introduction</b>	<b>1</b>
1.1 electron dynamics in solids . . . . .	1
1.2 attosecond transient absorption spectroscopy (ATAS) . . . . .	1
1.3 high harmonic generation . . . . .	1
1.3.1 three-step model . . . . .	1
1.3.2 phase matching . . . . .	2
<b>2 Apparatus Design</b>	<b>3</b>
2.1 Introduction . . . . .	3
2.2 The Need for High Vacuum . . . . .	4
2.3 XUV Optics . . . . .	6
2.3.1 Fresnel Reflection from a Rough Surface . . . . .	8
2.3.2 Material Choice . . . . .	11
2.3.3 Angle Choice . . . . .	11
2.3.4 Roughness Choice . . . . .	13
2.3.5 XUV mirror choices . . . . .	13
2.3.6 entrance and exit arm length choice . . . . .	15
2.3.7 mirror physical dimensions choice . . . . .	15
2.4 HHG Gas Source . . . . .	15
2.4.1 Continuous Free Expansion Nozzle . . . . .	17
2.4.2 low pressure cell . . . . .	24
2.4.3 high pressure cell . . . . .	26
2.4.4 pulsed valve . . . . .	28
2.5 description of optical path . . . . .	28
2.5.1 general lab layout . . . . .	28
2.5.2 delay arm . . . . .	28

2.5.3	XUV arm . . . . .	28
2.5.4	IR diagnostic station . . . . .	28
<b>Appendix A Guidelines for using the TABLE</b>		<b>29</b>
A.1	OMRON Pump-down Procedure . . . . .	29
A.2	OMRON Venting Procedure . . . . .	31
A.3	Aligning the Interferometer . . . . .	32
A.3.1	the generation arm . . . . .	32
A.3.2	the pump arm . . . . .	32
A.3.3	finding spatial overlap . . . . .	32
A.3.4	finding temporal overlap . . . . .	32
A.4	Pointing into the Interferometer . . . . .	32
A.5	The High Pressure Cell (HPC) . . . . .	32
A.5.1	Introduction . . . . .	32
A.5.2	Initial Installation and Alignment . . . . .	33
A.5.3	Alignment with the HPC Installed . . . . .	40
A.5.4	Pump Down Procedure . . . . .	41
A.5.5	Startup and Shutdown . . . . .	42
A.6	Laser System Specifics . . . . .	42
A.6.1	The Spitfire . . . . .	42
A.6.2	Pointing Stabilization into the External Compressor . . . . .	42
A.6.3	The Spitfire's External Compressor . . . . .	42
A.6.4	The TOPAS-HE . . . . .	42
A.6.5	stability . . . . .	43
A.7	The Shutter System . . . . .	43
A.8	The Vacuum System . . . . .	43
A.9	Best practices: data acquisition . . . . .	43
A.10	Steve's sections . . . . .	43
<b>Bibliography</b>		<b>44</b>

# List of Figures

Figure	Page
1.1 3 step model from S. Schoun's thesis[10]. . . . .	1
2.1 Estimation of XUV propagation losses through 0.5 mm of air at STP. Atomic scattering data obtained from [4, 5]. Calculation follows Eqs. (2.1) to (2.3).	4
2.2 Estimation of XUV propagation losses through a vacuum level of $10^{-7}$ Torr and a distance of 4 meters. Transmission is well over 99.99% for this pressure-length product. Atomic scattering data obtained from [4, 5]. Calculation follows Eqs. (2.1) to (2.3). . . . .	5
2.3 Fresnel reflectance for s-polarized light on smooth metal mirrors at a grazing angle of 5 degrees. Refractive index data obtained from [4, 5]. Calculation follows Eqs. (2.10) and (2.11). . . . .	12
2.4 Fresnel reflectance for s-polarized light off a smooth gold mirror as a function of incident angle. Calculation follows Eqs. (2.10) and (2.11). . . . .	13
2.5 Effect of surface roughness on reflectance. Calculation follows Eq. (2.14). . .	14
2.6 The continuous free expansion nozzle. Gas flows from the base of the nozzle and out of the $200 \mu\text{m}$ aperture. The large through holes on the base of the nozzle are for mounting to the gas delivery system; the sidewall cuts are for clearance for other mounting hardware. The top surface is beveled to reduce the minimum allowable distance between the laser axis and the nozzle. . . . .	17
2.7 The structure of the supersonic gas plume after leaving a gas nozzle. This figure was taken from Ref [8]. . . . .	18
2.8 Centerline Mach number versus distance in nozzle diameters for 2D (planar) and 3D (axisymmetric) geometries, calculated using Eq. (2.23). . . . .	18
2.9 Free jet centerline properties versus distance in nozzle diameters for helium gas ( $\gamma=5/3$ , $W=4$ ). Mach number is calculated using Eq. (2.23), and the centerline properties are calculated using Eq. (2.21). Velocity $V$ is scaled by terminal velocity $V_\infty$ ; temperature $T$ , number density $n$ and pressure $P$ are normalized by source stagnation values $T_0$ , $n_0$ , $P_0$ . . . . .	19
2.10 Detail of the LPC interaction region. . . . .	24

2.11	Gas flow schematic of the LPC. The green arrows indicate the direction of gas flow, and the red shaded region indicates the laser path. An infinite reservoir of gas with backing pressure $P_0$ supplies the laser interaction region with gas via a thin capillary of diameter $d_0$ , length $L$ and throughput $T_{tube}$ . The interaction region has pressure $P_1$ and diameter $d_1$ . The interaction region acts as a pressure source for two diametrically opposed supersonic gas jets, each with throughput $T_{nozzle}$ . The generation chamber has a turbopump with pumping speed $S_{turbo}$ and an equilibrium pressure $P_{cham}$ .	25
2.12	Detail of the HPC interaction region. From bottom left to top right: welded gas feedthrough, concentric inner & outer pipes, edge-welded bellows. The high pressure region is shaded blue. The green lines indicate the gas flow direction; the red line indicates the laser propagation direction.	26
2.13	Schematic used to calculate the pressures inside the HPC and generation chamber. The dark blue region represents the inner pipe, the light blue region represents the outer pipe. Red arrows and text indicate gas sources, green arrows and text indicate flow towards the vacuum pumps; blue arrows and text indicate physical dimensions. $P_H$ , $P_M$ , and $P_L$ are the pressures of the inner pipe, outer pipe, and generation chamber, respectively; $S_{turbo}$ , $S_{eff}$ and $C_{annular}$ are the turbo pumping speed, effective rough pumping speed and annular conductance, respectively; $T_H$ ( $T_M$ ) is the gas throughput from the high (medium) pressure region into the medium (low) pressure region.	27
A.1	Exterior view of the generation chamber with the HPC installed showing the ancillary vacuum hardware. Red arrow indicates input laser path; green arrow points towards the HPC's RV pump.	33
A.2	The HPC with bracket installed on the XYZ translation stage, configured for the generation chamber. The hose clamp and gas supply tube is omitted from this drawing for clarity.	34
A.3	Laser filament in the aligned outer pipe of the HPC. The inner pipe is not yet installed. Alignment of the outer pipe is done at very low intensities; after alignment the power was increased to create a filament for illustrative purposes only. This picture was taken in the target chamber during the initial testing of the HPC. The geometry of this chamber requires that the orientation of the mounting bracket is reversed compared to what is shown in Fig A.2.	35
A.4	Laser drilling the inner pipe. A card blocks the laser after exiting the HPC. The HPC was pressurized with Ar gas to enhance the filament for illustrative purposes.	36



# Chapter 1

## INTRODUCTION

### 1.1 electron dynamics in solids

### 1.2 attosecond transient absorption spectroscopy (ATAS)

general description of ATAS

### 1.3 high harmonic generation

#### 1.3.1 three-step model

single atom response

cycle-averaged quiver energy

$$U_p = \frac{q_e^2 F_0^2}{4m_e \omega^2} \propto I_0 \lambda^2 \quad (1.1)$$

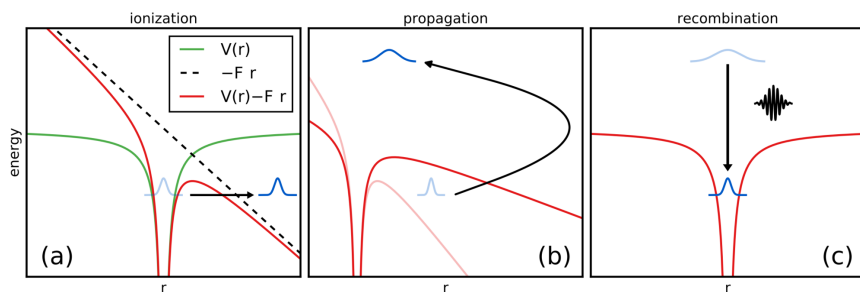


Figure 1.1: 3 step model from S. Schoun's thesis[10].

cutoff energy:

$$\omega_{cutoff} = I_p + 3.17U_p \quad (1.2)$$

semi-classical three step model

### 1.3.2 phase matching

macroscopic response

things i need to talk about:

$$\Delta k = \Delta k_{atomic} + \Delta k_{plasma} + \Delta k_{Gouy} + \Delta k_{dipole} \quad (1.3)$$

### 1D phase matching model

for the  $q^{th}$  harmonic, the number  $N_{out}$  of photons emitted on axis per unit time and of area is proportional to [1]:

$$\rho^2 A_q^2 \frac{4L_{abs}^2}{1 + 4\pi^2(L_{abs}^2/L_{coh}^2)} \left[ 1 + \exp\left(-\frac{L_{med}}{L_{abs}}\right) - 2 \exp\left(\frac{\pi L_{med}}{L_{coh}}\right) \exp\left(-\frac{L_{med}}{2L_{abs}}\right) \right] \quad (1.4)$$

where  $L_{coh} = \pi/\Delta k$  is the coherence length ( $\Delta k = k_q - qk_0$ )

- critical phase matching pressure (kazamias?)

# Chapter 2

## APPARATUS DESIGN

### 2.1 Introduction

what will be discussed in this chapter?

- the need for high vacuum
- all about XUV optics
- recombination mirror (hole mirror)
- modular design for beamline
- HHG gas sources (nozzle, LPC, HPC, pulsed valve)
- description of optical path

All elements in the periodic table have at least one electronic transition between 30 and 500 eV. Each transition has a characteristic photoabsorption cross section line shape, resulting in poor (good) transmission above (below) the transition. In the terminology of x-ray spectroscopy, this spectroscopic feature is called an *x-ray absorption edge*. Typical attenuation lengths<sup>1</sup> for most elements near an edge at energies of interest to our lab are measured in the tens of nanometers.

This basic feature of XUV light-matter interaction is both a blessing and a curse. On one hand, we can exploit the strong absorption to perform element-specific transient absorption

<sup>1</sup>The attenuation length is defined as the depth into the material measured along the surface normal where the intensity of x-rays falls to  $1/e$  of its value at the surface.

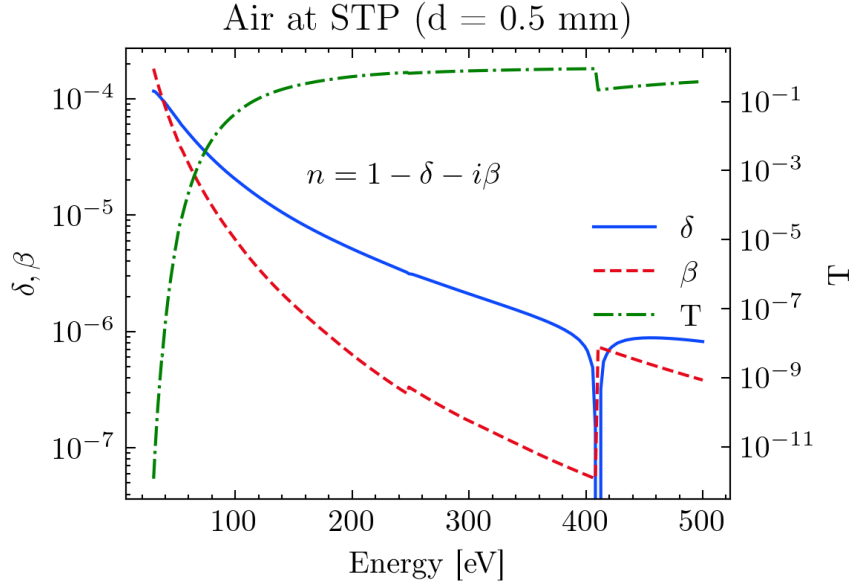


Figure 2.1: Estimation of XUV propagation losses through 0.5 mm of air at STP. Atomic scattering data obtained from [4, 5]. Calculation follows Eqs. (2.1) to (2.3).

spectroscopy on a myriad of elements and compounds (materials science permitting). On the other hand, the strong absorption puts severe experimental limits on any apparatus that uses XUV.

## 2.2 The Need for High Vacuum

The light generated by the high harmonic process is absorbed strongly by air, as most gases have at least one electronic transition in the XUV regime. The magnitude of absorption can be estimated using the atomic scattering factors  $f = f_1 + if_2$ , which were taken from [5]. The photoabsorption cross section  $\mu_a$ , the transmission ratio  $T$ , and the complex index of refraction  $\hat{n}$  of a gas can be calculated from these factors:

$$\mu_a = 2r_0\lambda f_2 \quad (2.1)$$

$$T = \exp(-N\mu_a d) \quad (2.2)$$

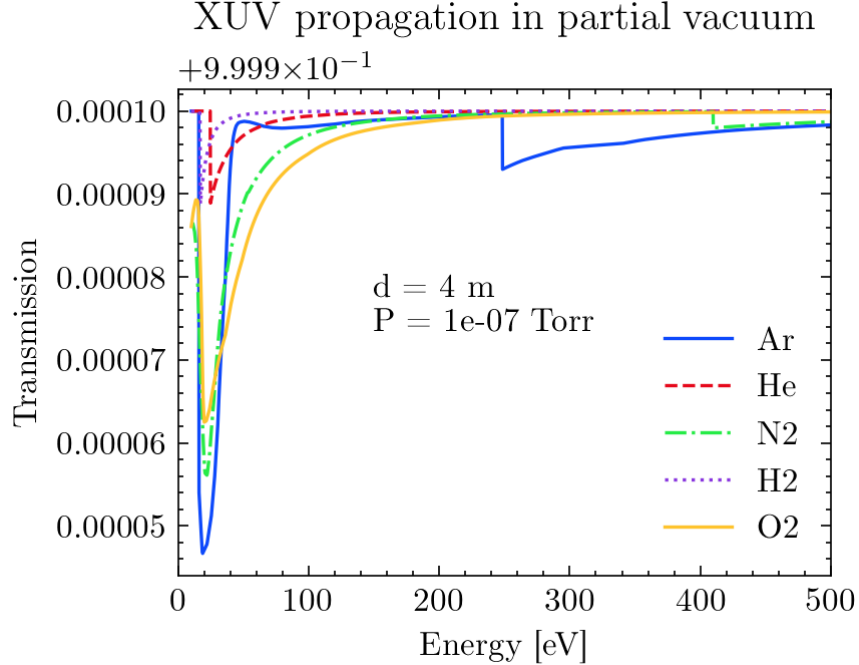


Figure 2.2: Estimation of XUV propagation losses through a vacuum level of  $10^{-7}$  Torr and a distance of 4 meters. Transmission is well over 99.99% for this pressure-length product. Atomic scattering data obtained from [4, 5]. Calculation follows Eqs. (2.1) to (2.3).

$$\hat{n} = 1 - \frac{1}{2\pi} N r_0 \lambda^2 (f_1 + i f_2) \quad (2.3)$$

In the above equations,  $\lambda$  is the photon wavelength,  $N$  is the number of atoms per unit volume,  $d$  is the optical path length and  $r_0 = 2.8179403227(19) \times 10^{-6}$  nm is the classical electron radius. The results for air at standard temperature and pressure are shown in Fig. 2.1. From this figure it is apparent that any XUV light we generate will be effectively attenuated to zero in less than 1 millimeter if the beam is propagated in air.

For reference, the XUV portion of the transient absorption beamline is about 4 meters long. Fig. 2.2 shows the expected XUV transmission losses for XUV propagation through a partial vacuum of common gases: argon and helium are often used for generation, while nitrogen, hydrogen and oxygen are common UHV system contaminants. From this figure, we can see that the XUV transmission exceeds 99.99% for an average pressure of  $10^{-7}$  Torr. Note that this calculation does not include reflection losses from the ellipsoidal mirror,

which are on the order of 10%. This simple analysis tells us that the XUV portion of the beamline must be kept under relatively high vacuum to avoid needlessly reducing the XUV flux.

The microchannel plate (MCP) assembly in the photon spectrometer puts additional constraints on the vacuum level. Contaminants in the spectrometer chamber lower the effective electrical resistance between the highly charged plates, resulting in a somewhat periodic current surge between the plates. This effect manifests itself in the data as a bright point source at a random location on the detector. In addition to reducing the fidelity of the data, each current surge counts towards the lifetime limit of the MCP assembly, reducing its lifetime [7].

The low pressure condition required to minimize XUV absorption and instrumentation malfunction is in direct conflict with the requirements for high harmonic generation (HHG) and gas-phase attosecond transient absorption spectroscopy (ATAS) experiment. HHG requires a gas source to be placed near the IR focus in the generation chamber, and a gas-phase ATAS experiment requires a similar gas source to be placed near the XUV/IR focus in the target chamber. The gas from these sources will diffuse into neighboring chambers, raising the pressure of the entire beamline. The vacuum system was designed to localize the gas density at the interaction regions while allowing a range of optical configurations to be used.

- modular endstation design
- in-air convenience
  - split level table
  - magnetic turbo pumps

## 2.3 XUV Optics

The XUV light is divergent after its generation and needs to be focused onto a sample for the experiment. The short relatively wavelength of the XUV puts strong requirements on the surface quality of the focusing optic, raising the cost and manufacturing time significantly.

Alignment of the optic is frustrated by the need for in-vacuum propagation and the invisible nature of XUV light. These factors lead us to pursue a "one size fits all" broadband optic rather than a series of interchangeable narrow bandwidth optics tailored for individual experiments.

The presence of strong absorption edges over the bandwidth of the XUV pulse precludes the use of transmissive optics. Narrow bandwidth transmissive optics have been designed to exploit the dispersion near an absorption edge [2]. However, these techniques cannot be extended to support the entire bandwidth of our XUV pulses. Reflective dielectric coatings have been designed for the XUV (**citation needed - Dietrich, Krauss?**), but their reflectance is only good for 10-20 eV (**need a source. this range might be incorrect.**). These considerations leave reflective optics as the only good choice for broadband XUV light.

The IR intensity profile at the focus is an important parameter for every experiment. In a transient absorption experiment, the experimental signal originates from the spatial overlap of the sample, the XUV and the IR light in the interaction region. Ideally, neither pulse would have any spatial structure at the interaction plane. In the real world, we design the optics to minimize the intensity variation of the IR over the spatial extent of the XUV spot. For finite beam sizes, this is accomplished by focusing the XUV tighter than the IR while minimizing aberrations. We chose to demagnify the XUV spot size by a factor of three, which reduces the XUV spot area by a factor of nine. This allows us to more strongly focus the IR pump pulse, resulting in a nine-fold increase of interaction intensity without changing the relative spot sizes of the XUV and the IR. While not required for a condensed matter experiment, the increased IR intensity was essential to doubly ionize helium gas for  $e - 2e$  experiments [6].

In the following sections, we outline the decision-making process for choosing an XUV optic. We start with a review of the physics of reflection from a rough metallic surface. Using these results we determine the optimal material, thickness, surface roughness and angle of the optic. We then compare the most common mirror configurations and discuss their suitability for a 3x demagnification. We conclude by describing

### 2.3.1 Fresnel Reflection from a Rough Surface

need a figure showing the interface, defining angles, indices, etc.

We use the familiar Fresnel equations to model reflection from the surface of a conductive surface [14]. In the equations that follow, the vacuum is denoted by  $j = 1$  and the conductive material is  $j = 2$ . The incident electric field is  $E_I$  and the reflected component is  $E_R$ . Following standard convention, the  $p$ -polarized light refers to light that has a polarization normal to the surface;  $s$ -polarized light is polarized parallel to the surface. The complex reflection amplitudes  $r_{s,p}$  are written in terms of the complex impedance  $\hat{Z}_j = \mu_j c / \hat{n}_j$  and the angle measured from the normal in each medium  $\theta_j$ :

$$\hat{r}_s \equiv \left[ \frac{E_R}{E_I} \right]_s = \frac{\hat{Z}_2 \cos \theta_1 - \hat{Z}_1 \cos \theta_2}{\hat{Z}_2 \cos \theta_1 + \hat{Z}_1 \cos \theta_2} \quad (2.4)$$

$$\hat{r}_p \equiv \left[ \frac{E_R}{E_I} \right]_p = \frac{\hat{Z}_1 \cos \theta_1 - \hat{Z}_2 \cos \theta_2}{\hat{Z}_1 \cos \theta_1 + \hat{Z}_2 \cos \theta_2} \quad (2.5)$$

Next, we assume non-magnetic media ( $\mu_1 = \mu_2 = \mu_0$ ) and write the amplitudes in terms of the complex indices of refraction  $\hat{n}_j = n_j + ik_j$ :

$$\hat{r}_s = \frac{\hat{n}_1 \cos \theta_1 - \hat{n}_2 \cos \theta_2}{\hat{n}_1 \cos \theta_1 + \hat{n}_2 \cos \theta_2} \quad (2.6)$$

$$\hat{r}_p = \frac{\hat{n}_1 \cos \theta_2 - \hat{n}_2 \cos \theta_1}{\hat{n}_1 \cos \theta_2 + \hat{n}_2 \cos \theta_1} \quad (2.7)$$

The reflectance is the modulus squared of the reflection amplitudes:

$$\hat{R}_s = \left| \frac{\hat{n}_1 \cos \theta_i - \hat{n}_2 \cos \theta_t}{\hat{n}_1 \cos \theta_i + \hat{n}_2 \cos \theta_t} \right|^2 \quad (2.8)$$

$$\hat{R}_p = \left| \frac{\hat{n}_1 \cos \theta_t - \hat{n}_2 \cos \theta_i}{\hat{n}_1 \cos \theta_t + \hat{n}_2 \cos \theta_i} \right|^2 \quad (2.9)$$

Finally, we assume that the first medium is vacuum ( $\hat{n}_1 = 1$ ) and apply Snell's law to write

the transmitted angle  $\theta_2$  in terms of the incident angle  $\theta_1$ :

$$\hat{R}_s = \left| \frac{\cos \theta_1 - \hat{n}_2 \sqrt{1 - \left( \frac{1}{n_2} \sin \theta_1 \right)^2}}{\cos \theta_1 + \hat{n}_2 \sqrt{1 - \left( \frac{1}{n_2} \sin \theta_1 \right)^2}} \right|^2 \quad (2.10)$$

$$\hat{R}_p = \left| \frac{\sqrt{1 - \left( \frac{1}{n_2} \sin \theta_1 \right)^2} - \hat{n}_2 \cos \theta_1}{\sqrt{1 - \left( \frac{1}{n_2} \sin \theta_1 \right)^2} + \hat{n}_2 \cos \theta_1} \right|^2 \quad (2.11)$$

The above analysis is valid for a perfectly smooth interface, but real optics have finite roughness. Loosely speaking, the surface roughness becomes important when it is on the order of the photon wavelength. As a point of comparison, a high quality off-the-shelf optic will have a surface roughness of  $\lambda/10 = 63.2\text{nm}$ , which is 5 times larger than the wavelength of a 100 eV photon. Clearly, we need specialized optics if we want to work in the XUV.

We will summarize the results of the analytic treatment of surface roughness in the literature [3, 11]. The surface roughness can be thought of as a local modulation  $\delta z(\vec{r})$  of the ideal interface height  $z(\vec{r})$  with a variance  $\langle z^2 \rangle$ , and a characteristic in-plane length scale  $\delta r$  over which the modulation occurs. There are two limiting cases to consider, based on the relative magnitudes of  $\delta r$  and the extinction length  $1/k_2$ . For reference, the extinction length is on the order of 1  $\mu\text{m}$  for hard x-rays, and about 10 nm for XUV light.

First, consider the case where the characteristic length scale of the roughness is much larger than the extinction length ( $\delta r \gg 1/k_2$ ). In this case, the local electric field can be expressed in the following form:

$$E_j(x, y) = \left( A_j^+ \exp(i k_{j,z} z) + A_j^- \exp(-i k_{j,z} z) \right) \exp(i \omega t - k_i \text{in} \parallel . r_{||}) \quad (2.12)$$

In Eq. (2.12),  $A_j^+(A_j^-)$  denotes the amplitude of the incoming (outgoing) wave and  $k_i \text{in} \parallel . r_{||} = k_j \cos \theta_j$  denotes ???.

Then, the incoming field does not

$$r^{rough} = \frac{\langle A_1^+ \rangle_x}{A_1^-} = r \langle \exp(2i k_{1,z} z) \rangle = r \exp(-2k_{1,z} \langle z^2 \rangle) \quad (2.13)$$

Eq. (2.13) is the Debye-Waller factor.

Then, the modulation is slow enough that there is a phase relationship between the incident and reflected fields over a large area. This is the Debye-Waller limit, and the reflectance is modified by a factor of  $\exp(-4k_1^2\langle z^2 \rangle)$ .

If the modulation length scale is much less than the extinction length ( $\delta r \ll 1/k_2$ ) then there is no short-scale correlations between the electric field and the roughness. This is the Croce-Nérot limit, and the reflectance is modified by a factor of  $\exp(-4k_1 k_2 \langle z^2 \rangle)$ .

For hard x-rays, the Nevot-Croce Surface roughness has the effect of reducing the reflectance by an exponential factor.

The finite surface roughness of a real mirror reduces the reflectance by a factor of  $\exp(-4k_1^2\sigma^2)$ , called the *Debye-Waller factor* [3]. Here,  $\sigma$  is the root-mean-square (rms) of the vertical roughness, and  $k_1$  is the normal component of the wave-vector in vacuum. The final result is below:

Combining Eqs. (2.10) and (2.11) with Eq. (2.13) yields the reflectance of a rough metallic surface:

$$\hat{R}_s = \left| \frac{\cos \theta_1 - \hat{n}_2 \sqrt{1 - \left( \frac{1}{n_2} \sin \theta_1 \right)^2}}{\cos \theta_1 + \hat{n}_2 \sqrt{1 - \left( \frac{1}{n_2} \sin \theta_1 \right)^2}} \right|^2 \left( \frac{2\pi\sigma \cos \theta_1}{\lambda} \right)^2 \quad (2.14)$$

$$\hat{R}_p = \left| \frac{\sqrt{1 - \left( \frac{1}{n_2} \sin \theta_1 \right)^2} - \hat{n}_2 \cos \theta_1}{\sqrt{1 - \left( \frac{1}{n_2} \sin \theta_1 \right)^2} + \hat{n}_2 \cos \theta_1} \right|^2 \left( \frac{2\pi\sigma \cos \theta_1}{\lambda} \right)^2 \quad (2.15)$$

The mid spatial frequency roughness (MSFR) of the ellipsoidal mirror's surface is  $\leq 0.3$  nm when sampled at a spatial frequency of 1-200  $\mu m$ .

The extinction length in gold is on the order of 10 nm for photon energies below 500 eV. This length scale is much smaller than the spatial variation of the height of our ellipsoidal mirror (1 - 200  $\mu m$ ), so we treat the using the Debye-Waller factor [3, 12]:

$$r^{rough} = r^{smooth} \exp(-2k_{z,0}k_{z,1}\sigma^2) \quad (2.16)$$

- the extinction length for photon range 30 - 500 eV in gold is on the order of 0.07 - 0.2 nm.
- the 0.3 nm rms roughness is based on a measurement frequency of 1 - 200 microns. this corresponds to a relatively long-range / slowly varying roughness.
- therefore we should use the debye-waller factor.

Nevot-Croce model assumes random vertical roughness with a Gaussian distribution. for the low spatial frequencies of the roughness spectrum, the Fresnel reflection coefficient is usually multiplied with a Debye-Waller factor  $\exp(-16\pi^2 k_1^2 \sigma^2)$ , while for the high spatial frequencies, the correction coefficient is given by the Nevot-Croce correction factor  $\exp(-16\pi^2 k_1 k_2 \sigma^2)$ , where  $\sigma$  is the root-mean-square (rms) of the vertical roughness, and  $k_1$  and  $k_2$  are the normal components of the wave-vectors in the two media [12].

FRED calculations: toroid demagnification vs ellipsoid demagnification

why an ellipsoid doesn't have aberrations

aligning the ellipsoidal mirror - what the spot looks like when misaligned

### 2.3.2 Material Choice

**Fig. 2.3 needs more materials. include aluminum.**

Fig. 2.3 shows the Fresnel reflectance from various materials with an ideal interface at fixed angle.

We compare two common materials.

gold was chosen due to its chemical inertness and generally good reflectivity.

thickness of gold layer – penetration depth (in general and at 5 degrees)

40 nm of gold with a sticking layer ... explain your reasoning

### 2.3.3 Angle Choice

why did we go with 5 degrees?

footprint of beam on the optic / size of the optic [3]:

$$F = \frac{t_1}{\sin \alpha} t_2 \quad (2.17)$$

in the above equation,  $t_1, t_2$  are the rectangular dimensions of the input beam and  $\alpha$  is the

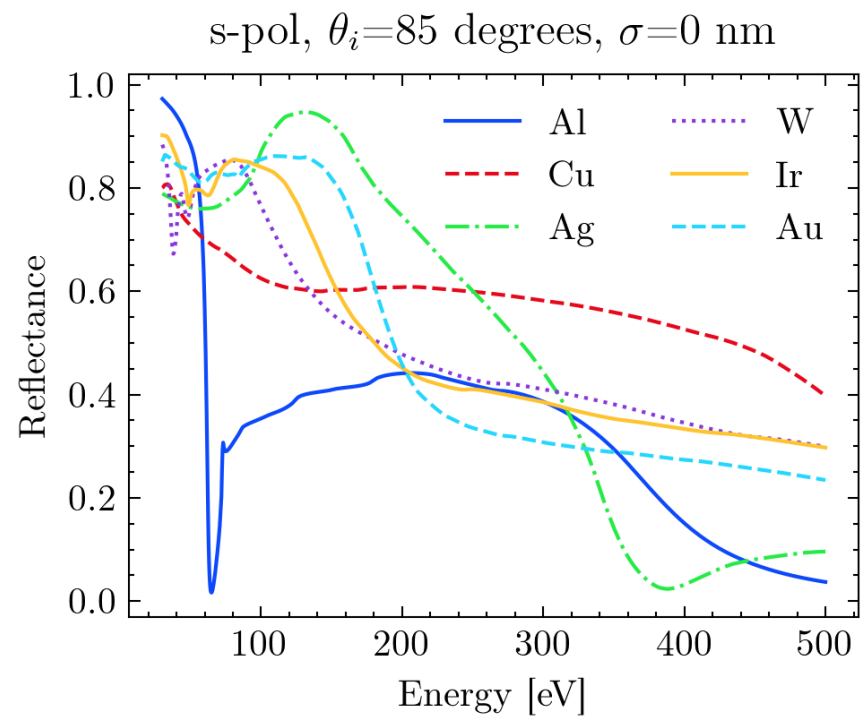


Figure 2.3: Fresnel reflectance for s-polarized light on smooth metal mirrors at a grazing angle of 5 degrees. Refractive index data obtained from [4, 5]. Calculation follows Eqs. (2.10) and (2.11).

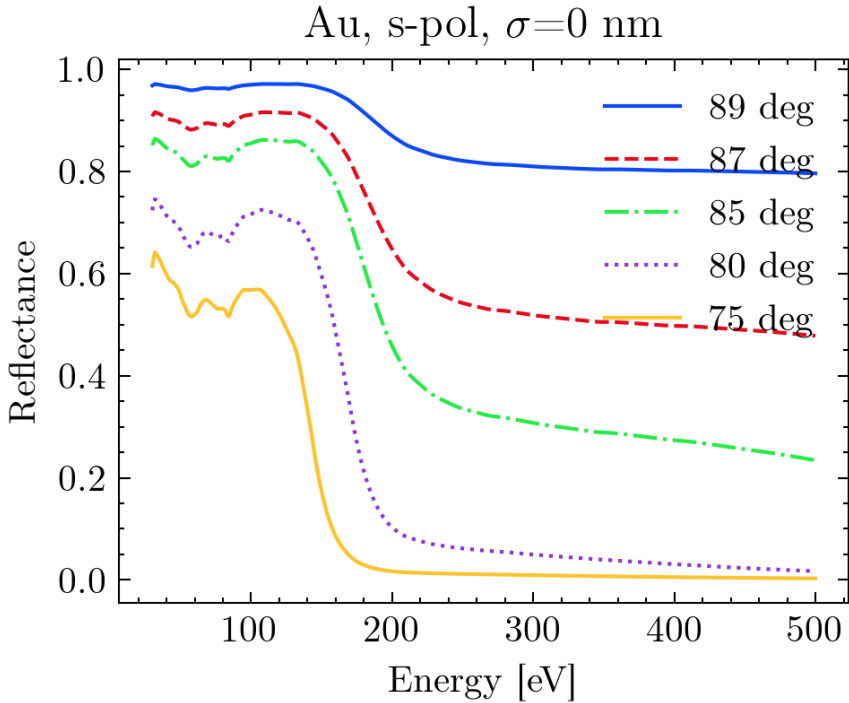


Figure 2.4: Fresnel reflectance for *s*-polarized light off a smooth gold mirror as a function of incident angle. Calculation follows Eqs. (2.10) and (2.11).

incident angle of the light on the mirror's surface. then  $F$  is the footprint of the beam on the angled mirror.

5 degrees was a good compromise between reflectivity, footprint on optic, and footprint of optic

### 2.3.4 Roughness Choice

why did we go with 0.3 nm rms? because it was state of the art, and very close to the performance of a ideal/smooth surface

### 2.3.5 XUV mirror choices

#### KB pairs

geometric description

avoided due to size of optics

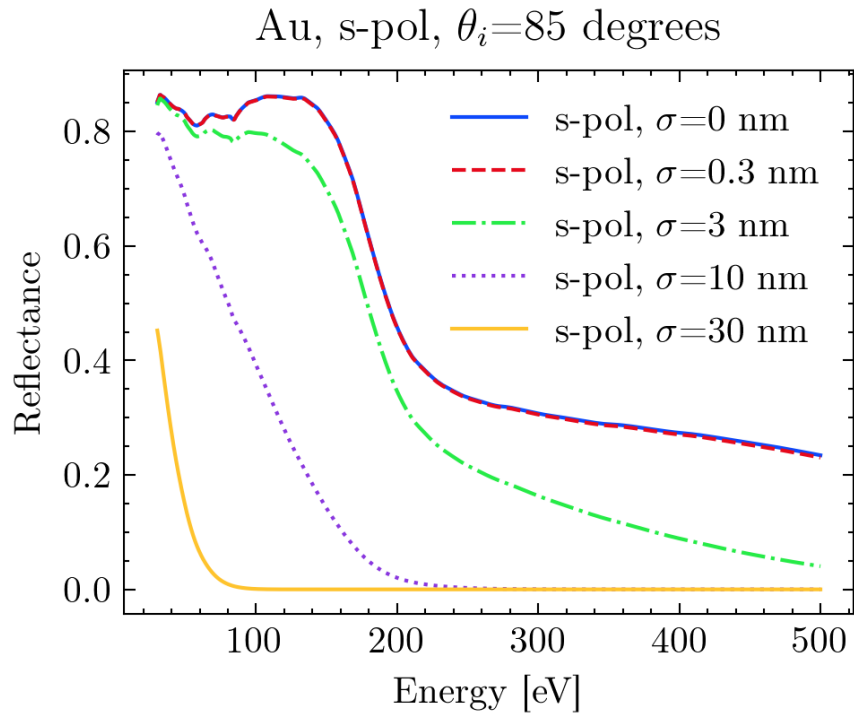


Figure 2.5: Effect of surface roughness on reflectance. Calculation follows Eq. (2.14).

disadvantage: multi-mirror configuration

### toroidal mirrors

geometric description of toroidal mirror, including equations / parameters

figure showing geometry

equal path length equations - choosing the optimal source, focal positions

coma and aberration when magnification is not unity

multi-mirror configurations (avoided due to complexity, size)

### ellipsoidal mirrors

geometric description, including equations. what parameters describe this optic?

figure showing geometry

coma and aberration are not an issue - why not?

advantage: single-mirror configuration

disadvantage: difficulty in manufacturing a non-spherical / non-cylindrical surface. solution: active

### 2.3.6 entrance and exit arm length choice

2250 mm entrance, 750 mm exit arm.

due to the modular nature of the beamline, we were limited on how short the exit arm could be. given the chamber geometries and the placement of the recombination optic, the exit arm had to be at least 750 mm.

### 2.3.7 mirror physical dimensions choice

this had to do with the assumed divergence of the XUV light and the entrance arm length.

## 2.4 HHG Gas Source

Transient absorption experiments require a high XUV photon flux for a variety of reasons. First, the sample thickness is usually chosen such that the XUV transmission is roughly 50% near the spectral feature of interest. This optical density represents a compromise between the incompatible goals of having a strong ground state absorption (which allows you to easily detect small changes in optical density) while simultaneously avoiding the noise floor of the detector (which is required for good statistics). As a result, half of the XUV photons will never reach the detector, so you better be making a lot of them. Second, a high XUV flux will reduce the number of laser shots required for a given data point, which in turn reduces the chances of inadvertently damaging your sample with the infrared laser. Finally, a high flux reduces the overall time required to complete an experiment. Besides the obvious benefit of happier graduate students, the ability to quickly perform an experiment increases data fidelity by reducing the effects of unavoidable experimental noise sources such as long-term laser drift (either pointing or energy) or environmental changes caused by the building's HVAC system.

Depending on the energy of the spectral feature, obtaining a high photon flux can range

from trivial to challenging. There are many (usually interdependent) experimental parameters (gas type, interaction pressure and length, wavelength, intensity, confocal parameter, focal position relative to gas source, etc.) that can be tuned to optimize photon flux. Physically, these parameters can change the microscopic single atom response, the macroscopic coherent addition of dipole emitters (via phase matching), or both. Each experiment will usually require a unique combination of experimental settings to achieve a usable light source. For example, optimizing the harmonic yield at 100 eV for a Si L-edge measurement will usually come at the expense of harmonics yield in the 30-50 eV range, which are used to measure the transition metal M-edges.

In general, an experimentalist has neither perfect knowledge nor control over all the variables that contribute towards phase matching. Setting aside the complicated topic of phase matching, the one dimensional on-axis phase matching model[1] shows that the photon flux is proportional to the square of the pressure-length product of the interaction gas. That is, so long as we can remain phase matched and below the critical phase matching pressure[9], we can universally increase the harmonic flux of our experiments by increasing the pressure-length product.

Unfortunately, one cannot ignore phase matching. Oftentimes, the spectral feature of interest lies beyond the harmonic cutoff when using the more convenient shorter wavelengths. In this case, the fundamental wavelength is increased to extend the cutoff (which scales as  $\lambda^2$ ). However, the critical phase matching pressure also scales as  $\lambda^2$  [9], and the single atom response scales as  $\lambda^{-(5-6)}$  [13]. These two combined effects result in a dramatically decreased photon flux if intensity and pressure are kept constant with increasing wavelength, often to the point that the resulting flux is insufficient for a transient absorption experiment, even though your cutoff has been extended to the proper energy. While some of the flux can be recovered by increasing the backing pressure of the continuous free expansion nozzle, the generation chamber's finite pumping speed limits the efficacy of pressure tuning at the longer wavelengths. Even at 800 nm, the maximum backing pressure of the continuous free expansion nozzle results in an interaction pressure below the critical phase matching pressure. Practically speaking, the continuous free expansion gas nozzle is not

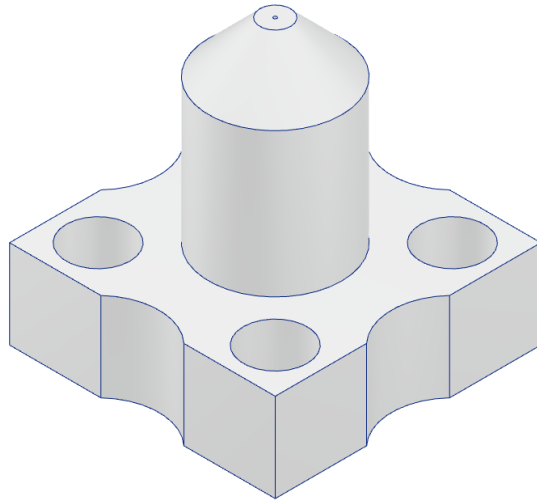


Figure 2.6: The continuous free expansion nozzle. Gas flows from the base of the nozzle and out of the  $200\ \mu\text{m}$  aperture. The large through holes on the base of the nozzle are for mounting to the gas delivery system; the sidewall cuts are for clearance for other mounting hardware. The top surface is beveled to reduce the minimum allowable distance between the laser axis and the nozzle.

suitable for transient absorption experiments using the signal wavelengths ( $\lambda > 1.6\ \mu\text{m}$ ) or with spectral features greater than the aluminum edge at 72 eV.

Providing the lab with a brighter harmonic source was the ultimate goal of the high pressure cell, and for the most part this goal was achieved. Below, we will review the basic design considerations, drawbacks and advantages of the three main types of gas sources used in this thesis: the free expansion nozzle, the low pressure cell and the high pressure cell. A primer on how to install and use the high pressure cell can be found in Appendix A.

#### 2.4.1 Continuous Free Expansion Nozzle

When gas flows from a high pressure region ( $P_0$ ) to a low pressure region ( $P_b$ ) through a small aperture, a plume will form in the low pressure region. If the pressure ratio  $P_0/P_b$  exceeds a critical value  $G \equiv ((\gamma+1)/2)^{\gamma/(\gamma-1)}$ , then the gas flow may exceed the local speed of sound. This critical value is at most 2.1 for all gases, so we easily exceed it in all of our

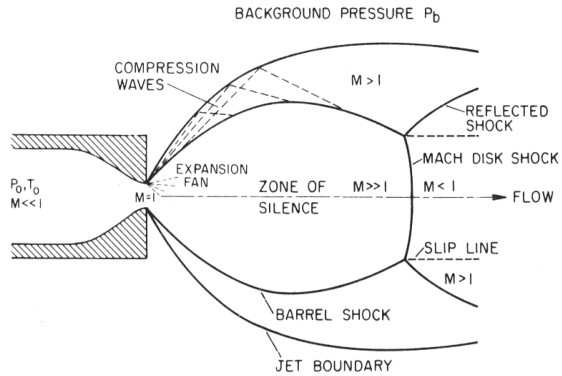


Figure 2.7: The structure of the supersonic gas plume after leaving a gas nozzle. This figure was taken from Ref [8].

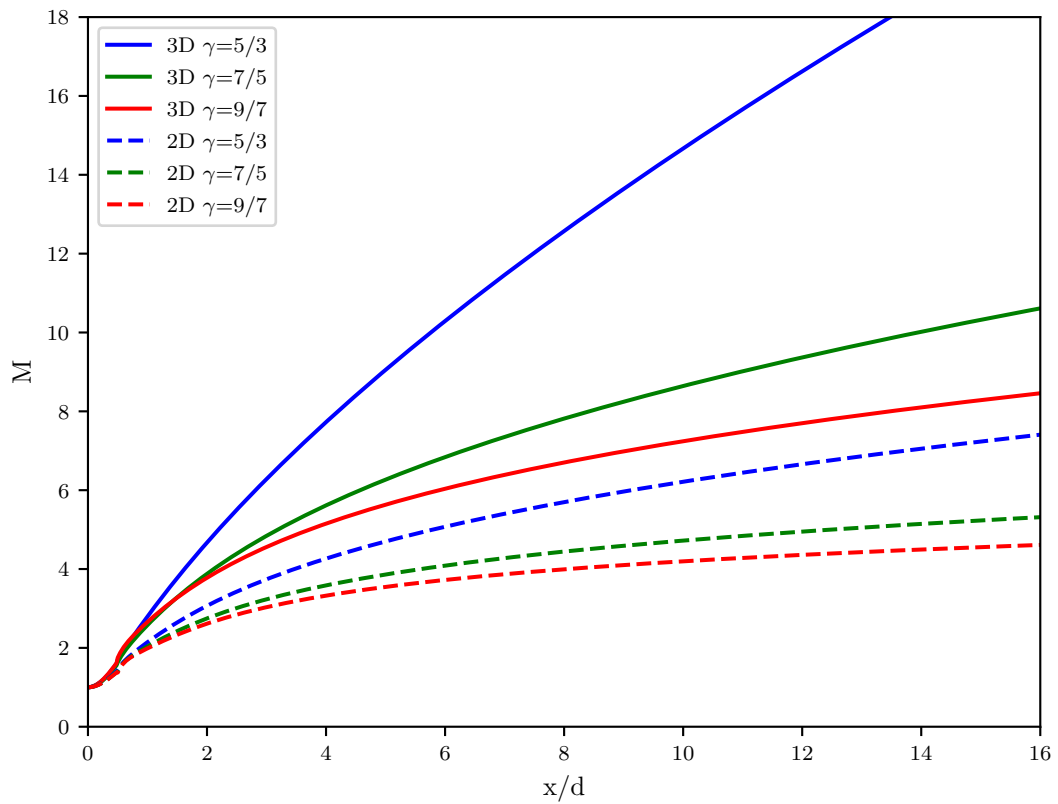


Figure 2.8: Centerline Mach number versus distance in nozzle diameters for 2D (planar) and 3D (axisymmetric) geometries, calculated using Eq. (2.23).

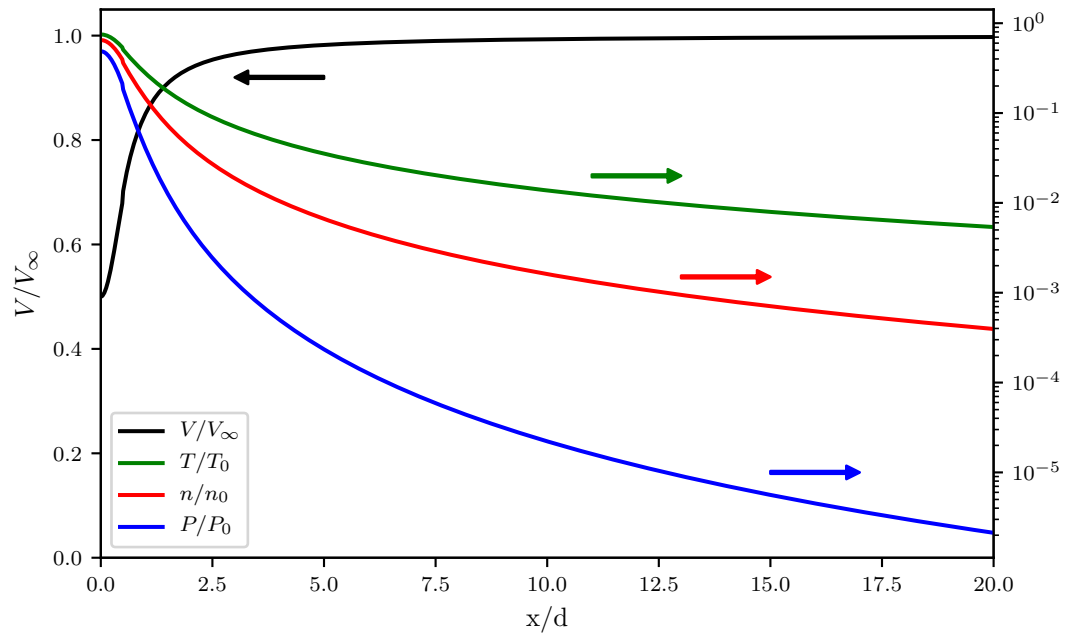


Figure 2.9: Free jet centerline properties versus distance in nozzle diameters for helium gas ( $\gamma=5/3$ ,  $W=4$ ). Mach number is calculated using Eq. (2.23), and the centerline properties are calculated using Eq. (2.21). Velocity  $V$  is scaled by terminal velocity  $V_\infty$ ; temperature  $T$ , number density  $n$  and pressure  $P$  are normalized by source stagnation values  $T_0$ ,  $n_0$ ,  $P_0$ .

experiments.<sup>2</sup> It is therefore necessary to understand the basic properties of supersonic gas plumes.

The continuous free expansion nozzle consists of a small diameter hole drilled in a block of aluminum, shaped to be convenient for gas delivery and assembly.<sup>3</sup> The basic design is shown in Fig. 2.6. The structure of the resulting supersonic plume is shown in Fig. 2.7. The physics of supersonic gas flow has been extensively studied in the literature and will not be discussed at length here. Below is a brief overview of the relevant physics required to understand the gas nozzles used for HHG in our lab. For a more detailed review of the field, see Ref [8].

energy equation.  $V$  is velocity,  $h$  is enthalpy per unit mass.

$$h + V^2/2 = h_0 \quad (2.18)$$

for ideal gases,  $dh = \hat{C}_p dt$ , and we have

$$V^2 = 2(h_0 - h) = 2 \int_T^{T_0} \hat{C}_p dT \quad (2.19)$$

For an ideal gas,  $\hat{C}_p = \gamma/(\gamma - 1)(R/W)$ , where  $\gamma = C_p/C_V$  is the ratio of the specific heats,  $R$  is the gas constant,  $W$  is the molecular weight. if the gas is cooled substantially in the expansion ( $T \ll T_0$ ), then we have:

$$V_\infty = \sqrt{\frac{2R}{W} \left( \frac{\gamma}{\gamma - 1} \right) T_0} \quad (2.20)$$

For an ideal gas, the speed of sound is  $a = \sqrt{\gamma RT/W}$  and the Mach number is  $M = V/a$ . Assuming  $\hat{C}_p$  is constant, we can recast Eq. (2.19) in terms of  $\gamma$  and  $M$ . Using these assumptions, one can obtain the following relationships for the temperature  $T$ , velocity  $V$ , pressure  $P$ , mass density  $\rho$  and number density  $n$  in the gas jet scaled to those parameters at the stagnation point ( $T_0, P_0, \rho_0, n_0$ ):

<sup>2</sup>The highest chamber pressures in our experiments are on the order of  $P_b \approx 10$  mTorr. Therefore, any nozzle that is backed by more than  $P_0 \approx 21$  mTorr will result in a supersonic gas flow. Typical backing pressures for harmonic generation are on the order of 250 Torr, putting us well within the supersonic regime.

<sup>3</sup>To reduce the gas load on the pumps, we used 200  $\mu\text{m}$  diameter nozzles. This was the smallest size hole the machine shop could readily drill into aluminum.

$$(T/T_0) = \left(1 + \frac{\gamma - 1}{2} M^2\right)^{-1} \quad (2.21a)$$

$$V = M \sqrt{\frac{\gamma R T_0}{W}} \left(1 + \frac{\gamma - 1}{2} M^2\right)^{-1/2} \quad (2.21b)$$

$$(P/P_0) = (T/T_0)^{\gamma/(\gamma-1)} = \left(1 + \frac{\gamma - 1}{2} M^2\right)^{-\gamma/(\gamma-1)} \quad (2.21c)$$

$$(\rho/\rho_0) = (n/n_0) = (T/T_0)^{1/(\gamma-1)} = \left(1 + \frac{\gamma - 1}{2} M^2\right)^{-1/(\gamma-1)} \quad (2.21d)$$

Therefore, once we know the Mach number  $M$ , we can calculate the above properties for the gas jet. The Mach number is found by solving the fluid mechanics equations dealing with the conversation of mass, momentum and energy:

$$\text{mass: } \nabla \cdot (\rho \mathbf{V}) = 0 \quad (2.22a)$$

$$\text{momentum: } \rho \mathbf{V} \cdot \nabla \mathbf{V} = -\nabla P \quad (2.22b)$$

$$\text{energy: } \mathbf{V} \cdot \nabla h_0 = 0 \text{ or } h_0 = \text{constant along streamlines} \quad (2.22c)$$

$$\text{equation of state: } P = \rho \frac{R}{W} T \quad (2.22d)$$

$$\text{thermal equation of state: } dh = \hat{C}_P dT \quad (2.22e)$$

The above equations are valid for an isentropic, compressible flow of a single component ideal gas molecular weight  $W$  and constant specific heat ratio  $\gamma$ . A steady state is assumed and viscosity and heat conduction are neglected. These equations have been numerically solved in the literature for two source geometries: a “slit” nozzle (2D, planar) and a circular aperture (3D, axisymmetric). The numerical solutions to each geometry scale with the nozzle diameter  $d$ , and have been fit to the following analytical functions:

$$\frac{x}{d} > 0.5 : \quad M = \left(\frac{x}{d}\right)^{(\gamma-1)/j} \left[ C_1 + \frac{C_2}{\left(\frac{x}{d}\right)} + \frac{C_3}{\left(\frac{x}{d}\right)^2} + \frac{C_4}{\left(\frac{x}{d}\right)^3} \right] \quad (2.23a)$$

$$0 < \frac{x}{d} < 1.0 : \quad M = 1.0 + A \left(\frac{x}{d}\right)^2 + B \left(\frac{x}{d}\right)^3 \quad (2.23b)$$

Source	$j$	$\gamma$	$C_1$	$C_2$	$C_3$	$C_4$	$A$	$B$
3D	1	5/3	3.232	-0.7563	0.3937	-0.0729	3.337	-1.541
3D	1	7/5	3.606	-1.742	0.9226	-0.2069	3.190	-1.610
3D	1	9/7	3.971	-2.327	1.326	-0.311	3.609	-1.950
2D	2	5/3	3.038	-1.629	0.9587	-0.2229	2.339	-1.194
2D	2	7/5	3.185	-2.195	1.391	-0.3436	2.261	-1.224
2D	2	9/7	3.252	-2.473	1.616	-0.4068	2.219	-1.231

Table 2.1: Gas parameters used in free expansion calculations, with Eq. (2.23). Table recreated from Ref [8].

**question: why does M increase without bound with increasing x, while V is limited to a finite value? scoles has a discussion, you should address it here.**

The fitting coefficients for Eq. (2.23) are listed in Table 2.1. A plot of the results for different source geometries and gases are shown in Fig. 2.8.

Table 2.3 shows the centerline Mach numbers used in the following equations:

$$M = A \left( \frac{x - x_0}{d} \right)^{\gamma-1} - \frac{\frac{1}{2} \left( \frac{\gamma+1}{\gamma-1} \right)}{A \left( \frac{x-x_0}{d} \right)^{\gamma-1}} \quad (2.24a)$$

$$\frac{\rho(y, x)}{\rho(0, x)} = \cos^2(\theta) \cos^2 \left( \frac{\pi\theta}{2\phi} \right) \quad (2.24b)$$

$$\frac{\rho(R, \theta)}{\rho(R, 0)} = \cos^2 \left( \frac{\pi\theta}{2\phi} \right) \quad (2.24c)$$

$$\left( \frac{x}{d} \right) > \left( \frac{x}{d} \right)_{\min} \quad (2.24d)$$

The gas nozzle throughput  $\hat{T}$  is calculated from:

$$\hat{T} \text{ (torr} \cdot \text{l/s}) = \hat{S} \cdot P_b = C \left( \frac{T_C}{T_0} \right) \sqrt{\frac{300}{T_0}} (P_0 d) d \quad (2.25)$$

where  $C$  is the gas constant from ??,  $P_0$  is the nozzle's backing pressure in Torr,  $T_C$  and  $T_0$  are the vacuum chamber and backing temperatures, respectively, in Kelvin,  $P_0$  is the backing pressure in Torr, and  $d$  is the nozzle's diameter in cm.

S = pumping speed? Pb = chamber pressure

(how was this equation derived?)

Gas	$\epsilon/k$ (K)	$\sigma$ (angstrom)	$C_6/k$ ( $10^{-43}$ K · cm <sup>6</sup> )	$Z_r$	C (l/cm <sup>2</sup> /s); Eq. (2.25)
He	10.9	2.66	0.154	-	45
Ne	43.8	2.75	0.758	-	20
Ar	144.4	3.33	7.88	-	14
Kr	190	3.59	16.3	-	9.8
Xe	163	4.3	41.2	-	7.9
H <sub>2</sub>	39.6	2.76	0.7	~300	60-63
D <sub>2</sub>	35.2	2.95	0.93	~200	42
N <sub>2</sub>	47.6	3.85	6.2	~2.5	16
CO	32.8	3.92	4.76	~4.5	16
CO <sub>2</sub>	190	4.0	31.1	~2.5	12-13
CH <sub>4</sub>	148	3.81	18.1	~15	21
O <sub>2</sub>	115	3.49	8.31	~2	15
F <sub>2</sub>	121	3.6	10.5	~3.5	14
I <sub>2</sub>	550	4.98	336	~1	5.2

Table 2.2: Gas parameters used in free expansion calculations. Table recreated from Ref [8].

Note that the gas nozzle throughput is proportional to both backing pressure and diameter of the nozzle. For our vacuum system, the generation chamber has a pumping speed of approximately ???;

Relevant gas parameters are listed in ??.

condition for supersonic flow: the pressure ratio  $P_0/P_b$  exceeds a critical value  $G \equiv ((\gamma + 1)/2)^{\gamma/(\gamma-1)}$ , which is less than 2.1 for all gases. Since the vacuum chamber pressure is at most 10 mTorr, just about any backing pressure will result in supersonic flow out of the gas nozzle.

Mach disk location:  $x_M/d = 0.67(P_0/P_b)^{1/2}$ . for example, for a chamber pressure of 10 mTorr and a backing pressure of -5 psig (~450 Torr), the Mach disk is located about 45 nozzle diameters away from the orifice. for a 200 micron diameter nozzle, that's about 9 cm.

basic design of free expansion nozzle

throughput calculations (Scoles)

harmonic yield results

$\gamma$	$x_0/d$	$A$	$\phi$	$(x/d)_{\min}$
1.67	0.075	3.26	1.365	2.5
1.40	0.4	3.65	1.662	6
1.2857	0.85	3.96	1.888	4
1.20	1.00	4.29	-	-
1.10	1.60	5.25	-	-
1.05	1.80	6.44	-	-

Table 2.3: Centerline Mach Number and Off-Axis Density Correlations for Axisymmetric Flow. Table recreated from Ref [8].

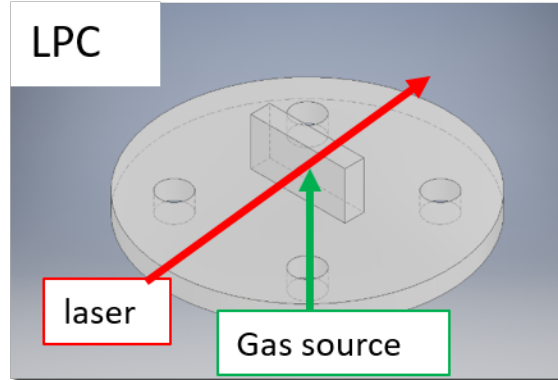


Figure 2.10: Detail of the LPC interaction region.

note: i did not design this cell

advantages: easy to align, cheap to produce, free-expansion cooling (for alignment experiments)

disadvantages: small pressure length product. very low interaction pressure. impossible to phase match longer wavelengths. overall low yield.

#### 2.4.2 low pressure cell

basic design of low pressure cell – gas load, Rayleigh range, spot size, laser drift

gas load calculations (simple model)

harmonic yield results

note that i did not design this cell. design is from (now Dr.) Zhou Wang.

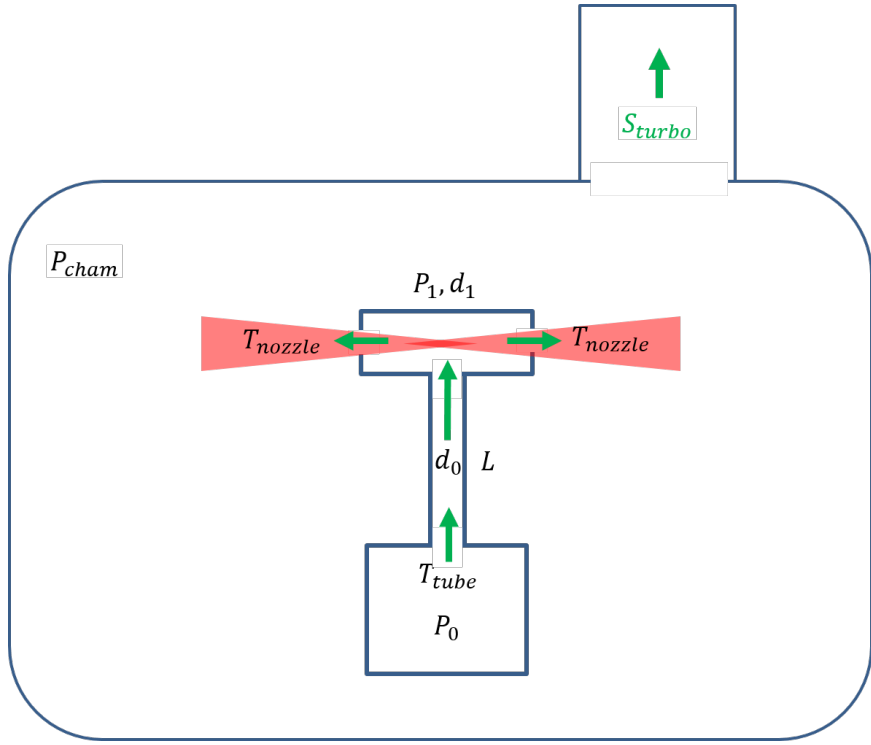


Figure 2.11: Gas flow schematic of the LPC. The green arrows indicate the direction of gas flow, and the red shaded region indicates the laser path. An infinite reservoir of gas with backing pressure  $P_0$  supplies the laser interaction region with gas via a thin capillary of diameter  $d_0$ , length  $L$  and throughput  $T_{tube}$ . The interaction region has pressure  $P_1$  and diameter  $d_1$ . The interaction region acts as a pressure source for two diametrically opposed supersonic gas jets, each with throughput  $T_{nozzle}$ . The generation chamber has a turbopump with pumping speed  $S_{turbo}$  and an equilibrium pressure  $P_{cham}$ .

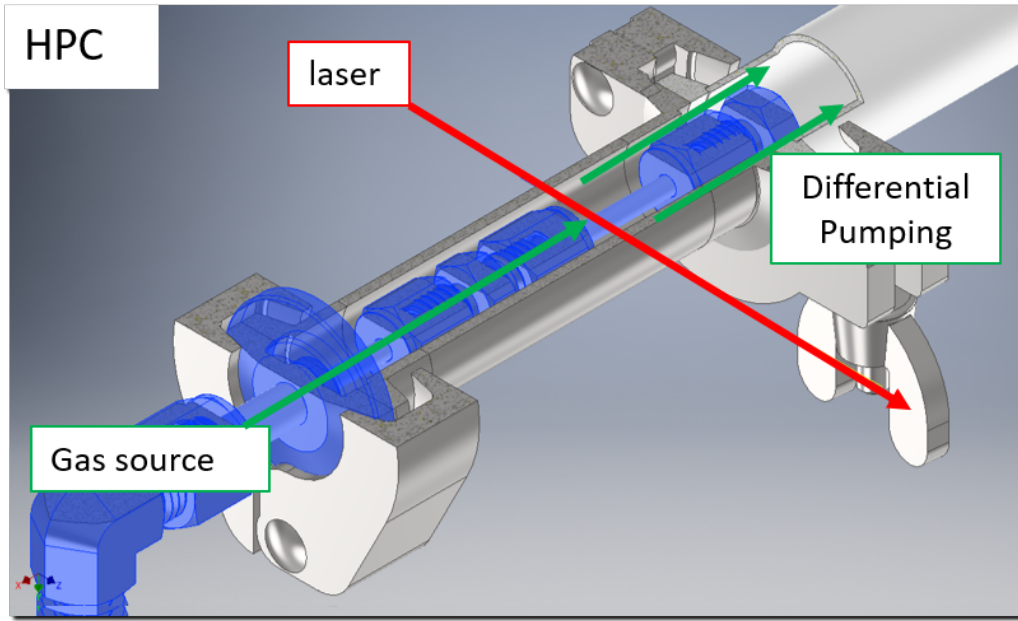


Figure 2.12: Detail of the HPC interaction region. From bottom left to top right: welded gas feedthrough, concentric inner & outer pipes, edge-welded bellows. The high pressure region is shaded blue. The green lines indicate the gas flow direction; the red line indicates the laser propagation direction.

advantages: increased interaction length - brighter! easy to align.

disadvantages: relative to the free expansion nozzle, you don't get any cooling.

#### 2.4.3 high pressure cell

- why didn't you go with semi-infinite gas cell, or fiber-cell?

- basic design of high pressure cell
- limited pump speed → differential pumping is required
- gas load calculations (simple model)

harmonic yield results

advantages: much brighter due to pressure-length product. future application: can operate in low-pressure mode and reduce downstream generation gas contamination of target chamber.

disadvantages: difficult to align and initially install (once it's installed, alignment is

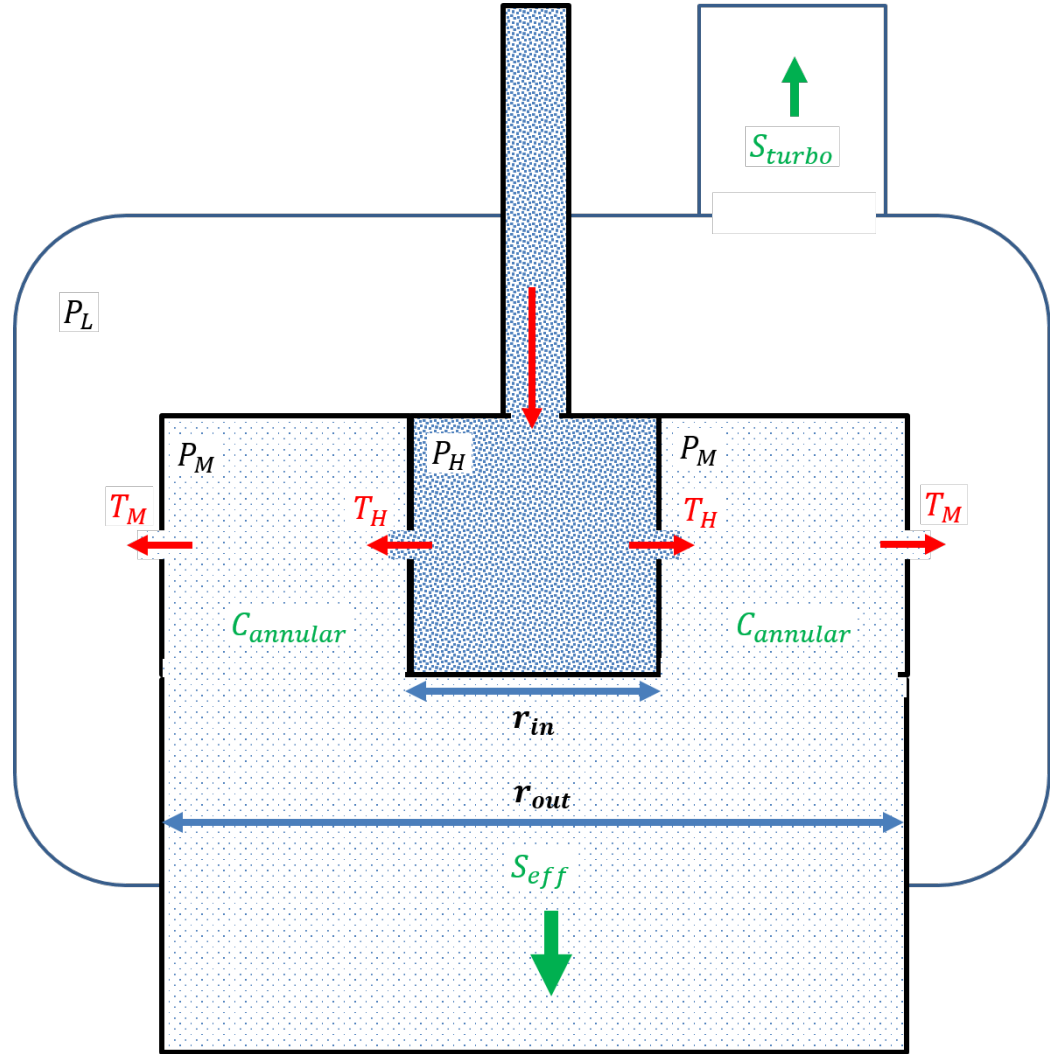


Figure 2.13: Schematic used to calculate the pressures inside the HPC and generation chamber. The dark blue region represents the inner pipe, the light blue region represents the outer pipe. Red arrows and text indicate gas sources, green arrows and text indicate flow towards the vacuum pumps; blue arrows and text indicate physical dimensions.  $P_H$ ,  $P_M$ , and  $P_L$  are the pressures of the inner pipe, outer pipe, and generation chamber, respectively;  $S_{turbo}$ ,  $S_{eff}$  and  $C_{annular}$  are the turbo pumping speed, effective rough pump speed and annular conductance, respectively;  $T_H$  ( $T_M$ ) is the gas throughput from the high (medium) pressure region into the medium (low) pressure region.

easy). messed up mode. HHG instability at higher pressures.

#### **2.4.4 pulsed valve**

expensive

### **2.5 description of optical path**

#### **2.5.1 general lab layout**

laser bay, target room. external compressor & TOPAS. automated pointing into compressor.

TABLe table.

#### **2.5.2 delay arm**

#### **2.5.3 XUV arm**

#### **2.5.4 IR diagnostic station**

# Appendix A

## GUIDELINES FOR USING THE TABLE

### A.1 OMRON Pump-down Procedure

Special thanks for Andrew Piper for coding and installing the `omron`safety system. Below is an operational guideline to pump the system down to UHV using the `omron`system. Please see Andrew Piper's `omron`manual for additional details on the microcontroller system.

This procedure assumes that the chambers are initially at atmospheric pressure, the rough pumps are turned on, and the solenoid shutoff valves on the roughing line are closed.

1. Seal and isolate all chambers. Close the manual hand valves between each turbo pump and the solenoid shutoff valves. Reattach any blow-off flanges (KF-25 blanks) that may have come off from the previous venting cycle.
2. Ensure the `omron`'s safety system is engaged by attempting to open one of the pneumatic gate valves via the control panel. **Caution: operating a gate valve between two chambers with a pressure differential can cause catastrophic system failure! Only perform this step after you have verified that all chambers are at atmospheric pressure!** If the gate valve opens while both chambers are above the upper setpoint, then the `omron` safety system has been disabled. Enable the safety system by switching the override switch to OFF.
3. Retract the metal filters from the beam path to protect them from potential pressure surges.

4. Initiate the pump-down sequence by pressing the OK button on the **OMRON**. This will open all solenoid valves simultaneously with a loud *thunk!*
5. Slowly open the manual handvalves while monitoring the pressure load on the rough pumps to avoid overloading the rough pump system. Use the two Raspberry Pi remote pressure monitoring systems to monitor the inlet pressure for each blower system. As a rule of thumb, try to keep the inlet pressure below  $\approx 100$  Torr during this step. **Warning: overloading the rough pumps will result in pump oil being expelled into the rough pump's exhaust line. Continuing to run in this condition can lead to overheating and eventually seizing of the rough pump.**
6. Once the hand valves are fully open on all chambers, you can turn each blower system ON to accelerate the remaining pump-down procedure.
7. Power on the turbo power supplies and switch the turbos to ON. After a few seconds, the magnetically levitated turbos will start levitating with a soft *thunk!*.
8. Each turbo will automatically start spinning when its chamber reaches the upper set point (about 200 mTorr). The turbos will take a few minutes to reach their final speed.
9. Wait for the system to pump down. It typically takes 15-45 minutes for the entire system to reach  $10^{-6}$  Torr.
10. The pneumatic gate valves for adjacent chambers will be enabled when both chambers are below their lower setpoint pressure (about  $5 \times 10^{-6}$  Torr). Once all chambers are below their lower setpoints, the **OMRON** considers the system is to be fully pumped down.
11. ARM each chamber by pressing ESC + [chamber number]. The **OMRON**'s display will update to show which chambers are armed (G: generation & differential pump chambers, M: mirror chamber, T: target chamber, S: photon spectrometer chamber).

## A.2 OMRON Venting Procedure

The **OMRON** system was designed with the ability to vent any single chamber or combination of chambers while keeping the others pumped down. This was a possibility when each chamber had its own rough pump, but now that the mirror, target & spectrometer chambers share a single blower system, extra care must be taken. **Any chambers that share a backing rough pump must be vented simultaneously to avoid turbopump overload.** For example, the mirror chamber, target chamber and spectrometer share a common blower system, and attempting to vent the one chamber while keeping the others will result in the spectrometer's turbo pump crashing due to the high backing pressure in the rough line.

This procedure assumes an initial condition of all chambers pumped down to UHV with the turbos running.

1. Turn off all gas sources / loads. If the HPC is installed, follow the HPC shutdown procedure.
2. Turn off the blowers.
3. Block the laser into the interferometer.
4. Close the pneumatic gate valves.
5. Disarm the chambers by pressing ESC + [chamber number].
6. Verify the **OMRON**'s safety system is not disabled by checking the bypass switch.
7. Enable the venting valves by switching ON the vent & purge controls on the control panel. The chambers will not vent without this step!
8. Remove the KF clamps on the blow-off valves.
9. Start the **OMRON** venting script by pressing ALT + [chamber number] on the **OMRON**.
10. The user can now walk away from the system. It will take a few hours to vent.

The venting script will immediately stop the turbopump's motors, open the solenoid venting valves after 30 seconds, close the roughing line's solenoid valves after 30 minutes, and close the solenoid venting valves after about 5 hours. The preceding timeline was chosen following the manufacturer's recommendation, and to avoid closing the roughing line's valves before the turbos had completely stopped spinning.

### A.3 Aligning the Interferometer

#### A.3.1 the generation arm

**The Ellipsoidal Mirror**

#### A.3.2 the pump arm

#### A.3.3 finding spatial overlap

#### A.3.4 finding temporal overlap

### A.4 Pointing into the Interferometer

the importance of pointing into the interferometer - spatial and temporal alignment

### A.5 The High Pressure Cell (HPC)

#### A.5.1 Introduction

*main text: description of the HPC's design, pressure & harmonic performance, pressure modeling, phase matching considerations. this section: how to install and actually use the HPC, how to machine or reorder certain parts.*

- focal length considerations. range of acceptable focal lengths. advantages of reflective vs transmissive focusing. possible schemes for shorter focal lengths.

- space constraints of TABLE generation chamber limit the size of the XYZ stack. these are Newport 9066 1/2" travel stages, with 1" travel thorlabs motors (that's what we had, ideally you would use 1/2" motors). as a result, you can accidentally drive the motor more than the stage will allow. this will result in the motor falling out of the stage. in this case,

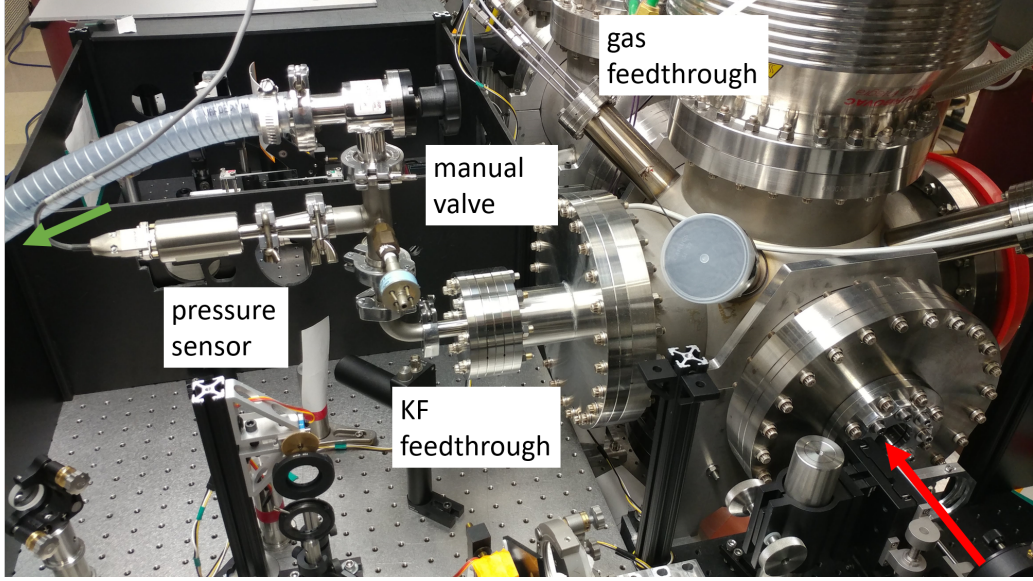


Figure A.1: Exterior view of the generation chamber with the HPC installed showing the ancillary vacuum hardware. Red arrow indicates input laser path; green arrow points towards the HPC's RV pump.

you will have to immediately block the laser, vent the chamber, and reattach the motor.  
note: travel of all motors is from 0 to 14 mm.

- in-vacuum manipulation via the vacuum bellows (limits of motion, max pressure differential)

The ancillary vacuum hardware can be seen in Fig A.1. A small oil-lubricated RV pump (not shown in this picture) provides differential pumping to the interior of the HPC. An inline Baratron diaphragm pressure sensor (effective range: 1 - 760 Torr) tracks the interior pressure of the edge-welded bellows. A manual gate valve is used to isolate the HPC from the RV pump when the additional pumping is not needed. Right angle KF fittings were used to route the HPC's vacuum line above the pump arm of the interferometer.

### A.5.2 Initial Installation and Alignment

First, a note about laser safety. The following alignment procedure should be done at the lowest possible laser power to minimize both accidental drilling of the HPC and the danger posed by stray light. Stray reflections or scatter from the many metallic surfaces of the HPC

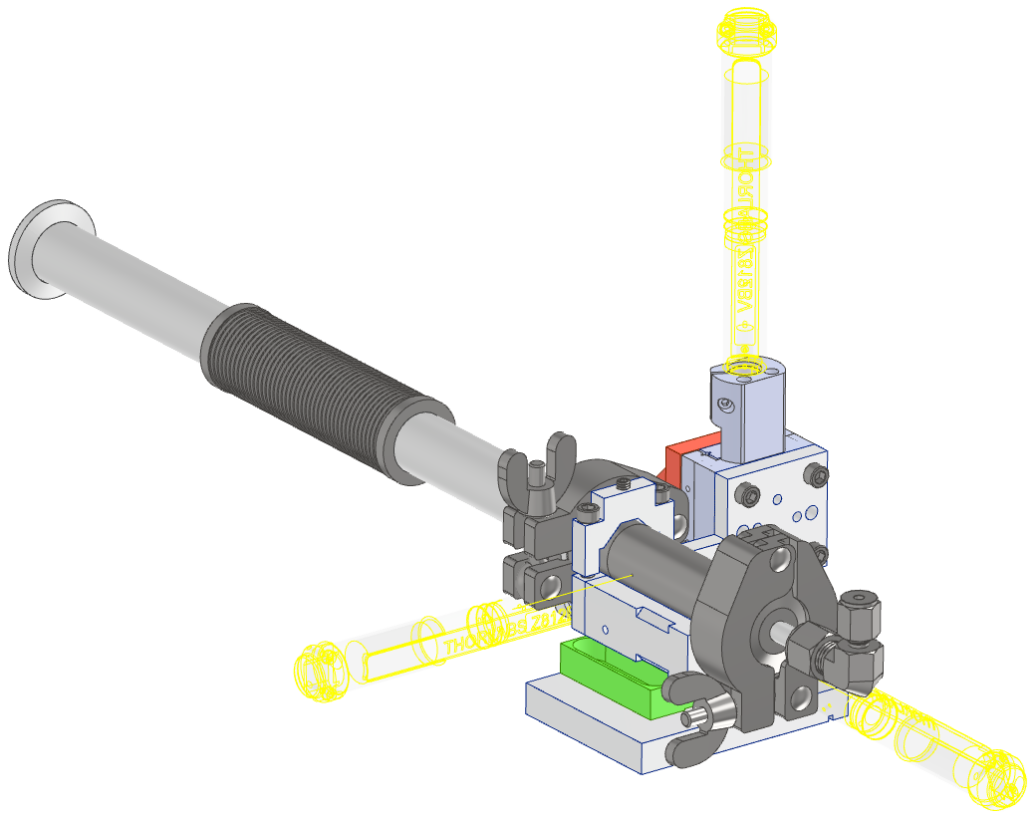


Figure A.2: The HPC with bracket installed on the XYZ translation stage, configured for the generation chamber. The hose clamp and gas supply tube is omitted from this drawing for clarity.

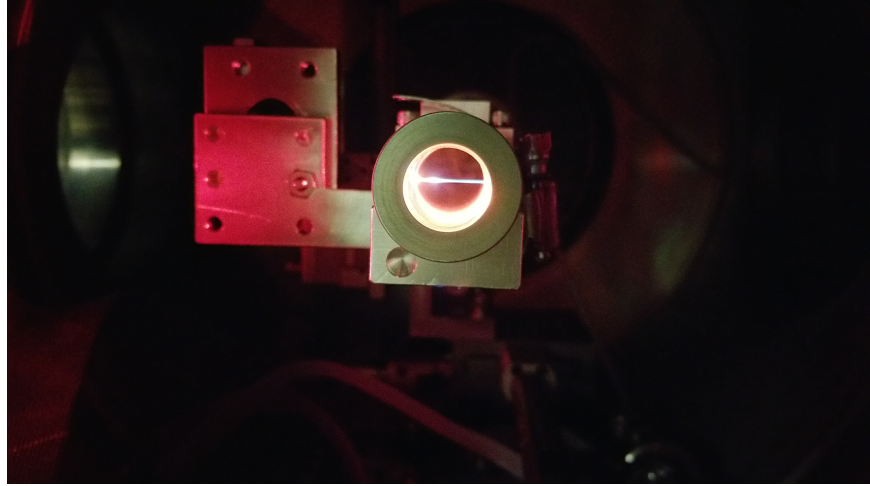


Figure A.3: Laser filament in the aligned outer pipe of the HPC. The inner pipe is not yet installed. Alignment of the outer pipe is done at very low intensities; after alignment the power was increased to create a filament for illustrative purposes only. This picture was taken in the target chamber during the initial testing of the HPC. The geometry of this chamber requires that the orientation of the mounting bracket is reversed compared to what is shown in Fig A.2.

assembly pose a potential safety risk during alignment. The surface most likely to cause laser scatter is the front face of the outer pipe, which is roughened stainless steel located about 3/8" before the focus. The material's roughness and the negative radius of curvature of the incoming light make it unlikely that incident light will coherently focus to a point upon reflection. However, it is possible that the sidewall of the outer pipe's aperture could act as a focusing mirror. Additionally, the hose clamp or mounting bracket could coherently reflect light towards the user. The user is advised to strictly follow all laser safety protocols during this alignment procedure. Whenever possible, direct observation of the laser beam on the surfaces of the HPC should be avoided, instead a webcam should be used to view the interior of the generation chamber.

The initial installation of the HPC can be time consuming and tedious, but once installed it will retain its alignment for a period of weeks or months. The pointing into the cell should be done on a daily basis, but this is only slightly more complicated than what must be done with a free expansion gas jet.

Optically, the HPC cell consists of four pinhole apertures (diametrically opposed pinholes

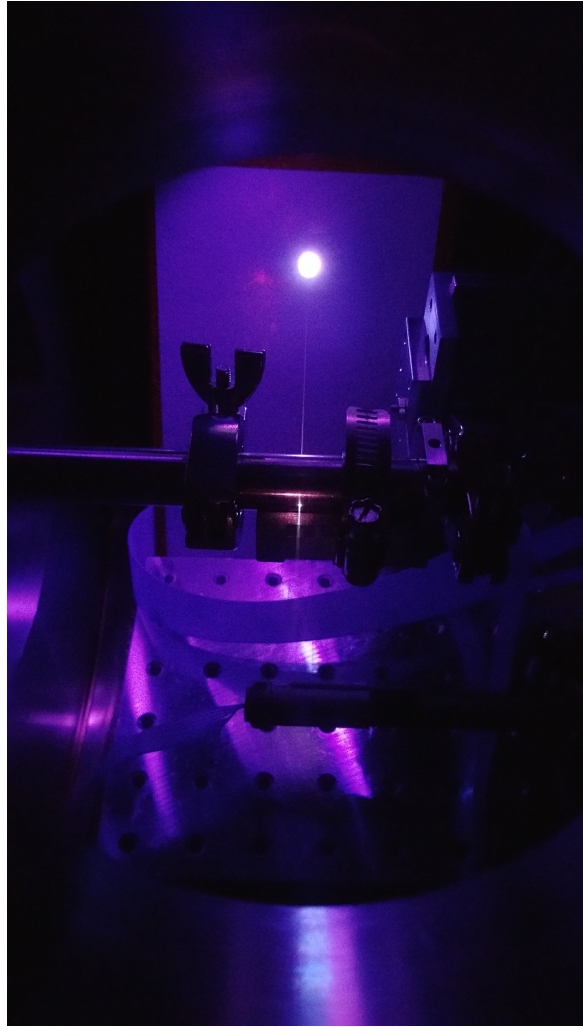


Figure A.4: Laser drilling the inner pipe. A card blocks the laser after exiting the HPC. The HPC was pressurized with Ar gas to enhance the filament for illustrative purposes.

on both the inner and outer pipes) with the laser focus near the center of the inner pipe. The optical transmission of the HPC is therefore very sensitive to the relative alignment of these components, as well as the pointing of the laser into the HPC. To simplify the alignment, the two innermost holes are laser drilled *in-situ* after the outer pipe has been aligned. To maintain the relative alignment of the inner & outer apertures, the user should refrain from adjusting the inner pipe after the initial alignment is completed. Therefore, daily alignment of the HPC should be performed using only the in-vacuum motorized XYZ stages.

The first step of the HPC installation is installing the rough vacuum feedthrough flange. The TABLE's generation chamber uses a custom flange (a 4.5" CF blank with a KF16 half nipple welded to the air-side and a KF16 bulkhead groove & tapped holes machined into the vacuum side). To accommodate the length of the in-vacuum bellows, we use a custom 10" CF to 4.5" CF reducing nipple (OAL = 4.25"), which acts as a spacer between the feedthrough flange and the KF16 flange on the HPC. Although it was absent from the original design, a spacer 4.5" CF flange (thickness = 0.68") between the feedthrough and the reducing full nipple is used to relax the compression in the bellows and allow for a larger range of motion. For convenience, the user should install the edge-welded bellows to the bulkhead flange before installing the flange on the chamber.

The supporting bracket for the HPC was designed to be interchangeable with the free gas nozzle's bracket. This design, shown in Fig. A.2, allows the user to change the gas source type without disturbing the alignment of the XYZ stage to the optical axis. For completeness, we will assume that the XYZ stage has been misaligned or removed from the chamber. First, the user should align the laser to the interferometer so that the laser path in the generation chamber can be used as a reference. Then, the stage should be positioned in the chamber so that the focus is roughly in the center of the stage's motion. Finally, the stage's z-direction should made parallel to the optic axis. This can be done by tracking the position of the laser on a card mounted to the stage while moving the stage upstream and downstream of the focus. After clamping the stage to the breadboard, check that the alignment is still true before continuing to the next step.

The next step is to align the outer pipe of the high pressure cell by maximizing its light transmission. This is best done in two steps: first, coarse alignment is done visually at low power (insufficiently intense to laser drill the pipe), followed by fine adjustments using a power meter at moderate intensities (above the noise floor of the power meter). Note that accidentally drilling out the outer pipe will reduce its differential pumping performance. Given the chamber's small size, it is not practical to place a power meter in the generation chamber after the focus during the alignment procedure. Rather, it is preferable to divert the beam out of the vacuum system using the linear actuator & silver mirror assembly located approximately 85 cm downstream of the focus.<sup>4</sup> When inserted, the linear actuator intersects the beam path and redirects the beam out of the vacuum system through a window onto the upper deck of the optical table. The beam size can be reduced using a focusing lens onto the face of a power meter. Note that for most generation focusing conditions, the large beam size at the diverting mirror makes this beam path lossy. To accurately calculate the transmission through the HPC, it is necessary to measure the power immediately after the HPC in the generation chamber.

For the coarse alignment, the input beam intensity should be reduced using an upstream iris, to the point that it is barely visible near the focus. Since a tightened KF connection prevents rotation of the components, the alignment of the outer piper is done prior to making any KF connections. However, the KF clamps should be fitted on either end of the pipe to ensure that there is enough room to make the connections without disturbing the alignment once finished. The outer pipe should be placed in its cradle, with the aluminum & hose clamps made snug around the pipe but not taut.<sup>5</sup> Transmission should be optimized by iteratively tuning the following parameters: (1) rotation of the pipe in the cradle, (2) height of the cradle using the vertical motor, and (3) horizontal (transverse) position of the assembly using both the horizontal motor and the position of the pipe in the cradle. For fine adjustment, the iris should be adjusted so that the power meter reads about 20-30

<sup>4</sup>Special thanks to Eric Moore for designing and installing this optomechanical component.

<sup>5</sup>The HPC's XYZ assembly and bracket were designed for the TABLE generation chamber. If it is being installed elsewhere, the user should verify that the height is correct. When installed correctly, the bottom of the Z-motor range should correspond to the HPC lowered completely out of the way of the laser; the top of the range should correspond to the laser going through the center of the HPC, with about 1 mm to spare.

mW when measured after the linear actuator.<sup>6</sup> The clamps should be tightened so that movement of the pipe is possible, but difficult. The area around the power meter should be covered to prevent air currents from affecting the measurement. The transmitted power should be optimized using the same procedure as before.

Once the outer pipe is aligned, tighten all connections and connect the bellows to the outer pipe. Check that the alignment has not been changed by torquing these connections. Verify that the unattenuated laser beam can pass through the outer pipe without interference, as shown in Fig. A.3. If everything looks good, we can proceed to install the inner pipe.

First, attach the gas delivery feedthrough flange onto the HPC assembly without the inner pipe. Being mindful to not disturb the alignment of the outer pipe, check that the gas delivery tubing does not interfere with the laser path. Remove the gas delivery feedthrough flange, cut the inner pipe to length (OAL = 1.75”), and make the Swagelok connection between the inner pipe and the KF feedthrough. Make sure the inner pipe is normal to the flange’s sealing surface, otherwise the laser will skim the sidewall of the inner pipe rather than go through the center. Install the gas delivery assembly onto the HPC assembly by tightening the KF clamp.

Laser drilling the inner pipe will sputter a significant amount of metal onto the inner surfaces of the chamber. Since the active drilling surface is on the upstream face of the pipe, most of the material will go upstream. Therefore, the laser window needs to be swapped out for a ”sacrificial” window prior to drilling.<sup>7</sup> Out of an abundance of caution, close the gate valve to the mirror chamber, retract the linear actuator & silver mirror from the beam path, and block the generation chamber’s vacuum aperture with a card.

Laser drilling should be done with the appropriate safety precautions: wearing laser goggles, notifying fellow labmates of your activity, and posting signs on the entrances to the

<sup>6</sup>This power is appropriate for a 1kHz repetition rate and a generation focal length of 30 or 40 cm.

<sup>7</sup>After drilling, the sacrificial window will be completely coated with a thin metal film. Most of the metal can be removed using methanol, but don’t expect to be able to use the window for anything but laser drilling. Using a window with different optical properties (i.e., thickness or material), or no window at all, will change the pointing and effective focal length of the beam. It has been suggested that the laser window could be protected by placing a thin sheet of transparent plastic (Saran Wrap) between the window and the HPC, but we haven’t tested this method.

lab. The user can cover up the chamber's flanges and set up a webcam to remotely monitor the laser drilling status to minimize the risk of inadvertent laser exposure.

At this point, the actual process of laser drilling is quite simple. There is no way to control the exact positioning of the inner pipe relative to the outer pipe, so there are no adjustments to make. Rather, the design relies on the mechanical alignment of the inner pipe relative to the outer pipe, which is ultimately set by the gas feedthrough weld, the Swagelok and the KF fitting. On the other hand, a used inner pipe cannot be reinstalled to the HPC once it is removed, since alignment is effectively impossible. To laser drill the pipe, simply let the unattenuated beam into the chamber and wait a few minutes until the laser emerges from the exit of the HPC. See Fig. [A.4](#).

If you are planning on scanning the k-direction of the HPC during an experiment, you should do so now while you are set up for laser drilling. Similarly, if you are using a non-reflective (achromatic) focusing scheme and are planning on changing wavelengths during your experiment (which will change the effective focal length), you should step through the full range of wavelengths while drilling. Doing so will open up the apertures slightly, resulting in additional metal deposition on the sacrificial laser window.

After laser drilling is complete, reinstall the laser window and verify the HPC has retained its alignment.

### A.5.3 Alignment with the HPC Installed

The daily pointing procedure, described in [A.4](#), is largely unchanged by the presence of the HPC. However, there are some extra considerations that need to be made if the HPC is installed. The small apertures of the HPC and the non-linear nature of HHG demand high accuracy in the pointing into the cell, so small corrections to the positioning of the HPC have to be made after the daily pointing procedure is completed.

#### Pointing into the Interferometer

If the interferometer is already aligned, the presence of the HPC does not really complicate the daily procedure of the beamline. In this case, the user should block the laser into the

generation chamber and align the pointing into the interferometer using the pump arm, as usual.<sup>8</sup> The procedure described in A.4 is sufficiently accurate to get the laser through the HPC, but it won't necessarily yield optimized harmonics. Rather, the user may have to make small tweaks to the transverse position of the HPC. This can be done by optimizing the harmonic flux by making small (10 - 25  $\mu\text{m}$ ) steps using both the vertical and horizontal HPC motors while monitoring the harmonic yield using a fast camera exposure ( $< 0.5$  s). In our experience, the optimal HPC position is typically within 50  $\mu\text{m}$  of the previous day's position.

The HPC's apertures may no longer be circular if the HPC has been subjected to accidental laser drilling or significant laser drift. Non-circular apertures may result in a complex spatial profile of the harmonics, which can make the optimization of the harmonic yield difficult.

### Aligning the Interferometer

If the interferometer needs to be realigned, then the HPC must be lowered out of the way of the laser. This is because the spatial mode of the IR is distorted by the HPC's apertures, which can introduce small shifts in the pointing of the IR after the HPC. Once the HPC is out of the way, the alignment procedure described in A.3 can be followed without modification. Unless major changes were made to the interferometer, the angle of the HPC's apertures should remain aligned to the k-vector of the generation arm. In this case, the optimal position of the HPC can be found by maximizing the transmitted power of an attenuated laser through the HPC, as described in the latter part of A.5.2. If major modifications were made to the interferometer, the user should consider aligning the HPC from scratch.

#### A.5.4 Pump Down Procedure

- pump down procedure
  - generating and optimizing harmonics

<sup>8</sup>Failure to block the laser prior to changing the pointing may result in laser-drilling the HPC.

- max internal pressure / pressure differential of the bellows tube
- max displacement of the tube

### A.5.5 Startup and Shutdown

## A.6 Laser System Specifics

importance of pointing & laser performance for our experiments

### A.6.1 The Spitfire

#### Regular Maintenance

- cleaning the stretcher
  - increasing the pump laser currents
  - changing the chiller fluid, desiccants, etc

#### quirks and features

- regen cavity tweaks
  - photodiode problems
  - software issues - bugs and troubleshooting

### A.6.2 Pointing Stabilization into the External Compressor

- dietrich plots for pointing

### A.6.3 The Spitfire's External Compressor

#### external compressor alignment

#### cleaning the grating

### A.6.4 The TOPAS-HE

- aligning - importance of power stability and pointing stability

### **A.6.5 stability**

- boxing things up - power stability throughout the day, people in the lab - unstable harmonic yield from the HPC at high pressures

### **A.7 The Shutter System**

### **A.8 The Vacuum System**

- blower upgrade
  - remote pressure sensing
  - vacuum calculations for steady state pressure of beamline

### **A.9 Best practices: data acquisition**

read-out noise from camera. (how noise scales)

### **A.10 Steve's sections**

steve - grating alignment (which axes do what to harmonics?)

steve - 2-source / phase plate stuff, including calibration

steve - operating the cage and crank

## BIBLIOGRAPHY

- [1] E. Constant, D. Garzella, P. Breger, E. Mével, C. Dorrer, C. Le Blanc, F. Salin, and P. Agostini. Optimizing High Harmonic Generation in Absorbing Gases: Model and Experiment. *Phys. Rev. Lett.*, 82(8):1668–1671, Feb. 1999.
- [2] L. Drescher, O. Kornilov, T. Witting, G. Reitsma, N. Monserud, A. Rouzée, J. Mikosch, M. J. J. Vrakking, and B. Schütte. Extreme-ultraviolet refractive optics. *Nature*, 564(7734):91, Dec. 2018.
- [3] A. Gibaud and G. Vignaud. Specular Reflectivity from Smooth and Rough Surfaces. In J. Daillant and A. Gibaud, editors, *X-Ray and Neutron Reflectivity: Principles and Applications*, Lecture Notes in Physics, pages 85–131. Springer Berlin Heidelberg, Berlin, Heidelberg, 2009.
- [4] E. Gullikson. CXRO X-Ray Interactions With Matter.  
[http://henke.lbl.gov/optical\\_constants/](http://henke.lbl.gov/optical_constants/).
- [5] B. L. Henke, E. M. Gullikson, and J. C. Davis. X-Ray Interactions: Photoabsorption, Scattering, Transmission, and Reflection at  $E = 50\text{-}30,000 \text{ eV}$ ,  $Z = 1\text{-}92$ . *Atomic Data and Nuclear Data Tables*, 54(2):181–342, July 1993.
- [6] D. Kiesewetter. *Dynamics of Near-Threshold Attosecond Electron Wavepackets in Strong Laser Fields*. Ph.D. thesis, The Ohio State University, Columbus, OH, 2019.
- [7] J. Ladislas Wiza. Microchannel plate detectors. *Nuclear Instruments and Methods*, 162(1):587–601, June 1979.

- [8] D. R. Miller. Free Jet Sources (Chap 2). In G. Scoles, editor, *Atomic and Molecular Beam Methods*, volume 1, pages 14–82. Oxford University Press, 1988.
- [9] T. Popmintchev, M.-C. Chen, A. Bahabad, M. Gerrity, P. Sidorenko, O. Cohen, I. P. Christov, M. M. Murnane, and H. C. Kapteyn. Phase matching of high harmonic generation in the soft and hard X-ray regions of the spectrum. *PNAS*, 106(26):10516–10521, June 2009.
- [10] S. B. Schoun. *Attosecond High-Harmonic Spectroscopy of Atoms and Molecules Using Mid-Infrared Sources*. Ph.D. thesis, The Ohio State University, Columbus, OH, 2015.
- [11] A. Sentenac and J. Daillant. Statistical Aspects of Wave Scattering at Rough Surfaces. In J. Daillant and A. Gibaud, editors, *X-Ray and Neutron Reflectivity: Principles and Applications*, Lecture Notes in Physics, pages 59–84. Springer Berlin Heidelberg, Berlin, Heidelberg, 2009.
- [12] K. N. Stoev and K. Sakurai. Review on grazing incidence X-ray spectrometry and reflectometry. *Spectrochimica Acta Part B: Atomic Spectroscopy*, 54(1):41–82, Jan. 1999.
- [13] J. Tate, T. Auguste, H. G. Muller, P. Salières, P. Agostini, and L. F. DiMauro. Scaling of Wave-Packet Dynamics in an Intense Midinfrared Field. *Phys. Rev. Lett.*, 98(1):013901, Jan. 2007.
- [14] A. Zangwill. *Modern Electrodynamics*. Cambridge University Press, Cambridge, 2013.